Thermo-biomechanical coupling analysis for preventing tomato fruit cracking during ripening

Thermo-biomechanical coupling analysis for preventing tomato fruit cracking during ripening

Huijie Liu[a], Pengfei Zhu[a], Zhiguo Li[a,*], Jianping Li [b, c,*], Fideline Tchuenbou-Magaia[d], Jiheng Ni[e]

[a]*College of Biomechanical and Electronic Engineering, Northwest A&F University, Yangling, Shaanxi 712100, China*

[b]*Key Laboratory of Equipment and Informatization in Environment Controlled Agriculture, Ministry of Agriculture and Rural Affairs, P.R. China*

[c]*College of Biosystems Engineering and Food Science, Zhejiang University, 866 Yuhangtang Road, Hangzhou 310058, China*

[d]*School of Engineering, Computing and Mathematical Sciences, Division of Chemical Engineering, University of Wolverhampton, Wolverhampton, WV1 1LY, UK*

[e]*Institute of Agricultural Engineering, Jiangsu University, Zhenjiang, 212002, China*

[*]*Correspondence Email: lizhiguo0821@163.com (Z. Li)*

Abstract: Fruit cracking is closely related to the heat transfer resulting from sunlight, so a thermo-biomechanical coupling three-point bending FE analysis in the tomato pericarp sample was performed. Results showed that the established FE model was capable of reproducing the experimental probe loading force-pericarp deflection and the crack propagation length-pericarp deflection curves in deflection deformation up to 6 mm, with average relative errors of 3.0 % and 4.3 %, respectively. The propagation area and volume of the crack in pericarp model were gradually sensitive to the temperature gradient acting on the exocarp surface and fruit ripeness. Three obtained linear mathematical models can quantitatively predict the cracking status of the pericarp under different temperature gradient levels when the sunlight caused a uniform temperature increase on the exocarp surface. The tomato had a better anti-cracking ability when the sunlight caused a non-uniform temperature increase on the exocarp surface. This study provides a basis for preventing the cracking of tomato fruit during development by controlling the environment.

Keywords: Fruit cracking; Heat transfer properties; Thermo-biomechanical couple; Temperature gradient; Finite element analysis

Nomenclature

C_p	heat capacity of pericarp, J kg^{-1} $^oC^{-1}$	T_1	dummy variable 1 of the temperature gradient
C_{ex}	heat capacity of exocarp, J kg^{-1} $^oC^{-1}$	T_2	dummy variable 2 of the temperature gradient
C_{me}	heat capacity of mesocarp, J kg^{-1} $^oC^{-1}$	T'	heat transfer rate
C_l	heat capacity of sapphire, J kg^{-1} $^oC^{-1}$	T_p	tomato pericarp temperature, °C
DSC_p	heat flow of pericarp, W g^{-1}	t	heat transfer time in the pericarp, s
DSC_l	heat flow of sapphire, W g^{-1}	V_c	total crack volume in pericarp model, mm^3
DSC_s	heat flow of empty crucible, W g^{-1}	v_{ex}	poisson's ratio of exocarp
E_{ex}	elastic modulus of exocarp, MPa	v_{me}	poisson's ratio of mesocarp
E_{me}	elastic modulus of mesocarp, MPa	$V_{iexbefore}$	volume of the i_{th} cracked element before crack propagation in the exocarp model
F	maximum loading force, N	$V_{jmebefo}$	volume of the i_{th} cracked element before crack propagation in the mesocarp model
f	number of cracked elements in the front view of the mesocarp model	$V_{iexafter}$	volume of the i_{th} cracked element after crack propagation in the exocarp model
G_{fex}	fracture energy of exocarp, mJ mm^{-2}	$V_{jmeafter}$	volume of the i_{th} cracked element after crack propagation in the mesocarp model
G_{fme}	fracture energy of mesocarp, mJ mm^{-2}	m	number of crack elements in mesocarp model
G	energy release rate	m_l	mass of the sapphire, mg
G_f	fracture energy, mJ mm^{-2}	m_p	mass of the pericarp, mg
K_{ex}	thermal conductivity of exocarp, W m^{-1} °C^{-1}	ρ_{e}	exocarp density, kg m^{-3}
K_{me}	thermal conductivity of mesocarp, W m^{-1} °C^{-1}	ρ_{m}	mesocarp density, kg m^{-3}
K	thermal conductivity of pericarp, W m^{-1} °C^{-1}	ρ	pericarp density, kg m^{-3}
k	number of crack elements in exocarp model	σ_{maxex}	fracture stress of exocarp, MPa
L_t	total crack length in the front view of the pericarp model, mm	σ_{maxme}	fracture stress of mesocarp, MPa
l_{ie}	crack length of the i_{th} cracked exocarp element, mm	σ_{max}	maximum principal stress at an element centroid
l_{im}	crack length of the i_{th} cracked mesocarp element, mm	σ_{max}^{a}	maximum allowable principal stress (failure stress)
L_d	pericarp deflection, mm	∇	gradient operator
q	heat flux of the elements in the tomato pericarp model	ΔT	temperature gradient acting on the exocarp surface, °C
N	the normal vector (dimensionless)	ΔT_i	increases uniform at the rate of exocarp surface temperature, °C
n	number of cracked elements in the front view of the exocarp model	$\Delta T_{1,2,3,4}$	increases non-uniformly at the rate of exocarp surface temperature, °C
Sc	total crack area in pericarp model, mm^2	RS	fruit ripening level
s_{ie}	crack area in the i_{th} cracked element of the exocarp model	RS_1	light - red stage
s_{jm}	crack area in the i_{th} cracked element of the mesocarp model	RS_2	riper than RS_1
S	center-point of the mesocarp model	x, y, z	Cartesian coordinate axis

1. Introduction

Cracking is a common phenomenon in fruit development and post-harvest processing, which seriously reduces fruit quality and marketability. Sunlight is the most important environmental factor inducing the biosynthesis of anthocyanin, flavanol, glucose and total sugar during fruit growth (Zoratti et al., 2014; Kawai et al., 2018), promoting lutein cycle (Ma and Cheng, 2004), and changing fruit weight, pericarp structure and soluble protein content (Woolf and Ferguson, 2000), but sometimes can cause some physiological diseases, especially fruit cracking (Morales-Quintana et al., 2020). After fruit surface cracks, the pericarp is extremely susceptible to be attacked by pathogenic bacteria and parasites and which leads to subsequent accelerated rot of the whole fruit. According to Chen et al. (2012), sunlight irradiation actually alters the temperature of fruit through heat transfer, which results in a temperature difference between different time periods during the day at the fruit surface as well as between the sun-exposed fruit surface and the shaded surface. This temperature difference in both regions with different sunlight intensity affects the texture mechanics, such as cuticle elasticity (Li et al., 2021), fruit elongation (Wala et al., 2022), and finally affects the quality and shape of fruits (Marsic et al., 2010). Therefore, it is important to investigate the biomechanical mechanism of tomato fruit cracking caused by sunlight.

Previous research on texture biomechanics of tomato fruit can be divided into two categories with focus on (1) the characterization of fruit thermo-mechanical properties and (2) the prediction of heat transfer behavior and fruit biomechanical response. Sangrame et al. (2000) proposed that the heat transfer coefficient, evaporation rate, and final concentration of tomato pulp varied within 625.6 ~ 910.9 W m^{-2} $°C^{-1}$, 13.22 ~33.72 kg h^{-1} and 8.02 ~ 19.21 %, respectively. Kumar et al. (2008) found that the heat transfer coefficient of tomato can be deduced by a temperature gradient inside the fruit during the cooling process. Lu et al. (2009) reported that the hot-air heat treatment can reduce the tomato fruit hardness and thermal conductivity is one of the main factors affecting the heat uniformity among fruits and inside individual fruit. Pek et al. (2011) found that the stronger the tomato is directly radiated by sunlight, the higher the fruit surface temperature rises, and the temperature of non-shaded fruit is higher than the air temperature in greenhouse. Yang et al. (2020) proposed that the magnetic field treatment can lower the hydrogen bond energy of water molecules in tomato skin and further change the skin density, heat transfer coefficient, specific heat capacity, and melting point. Gladyszewska et al. (2011) proposed that the difference between tomato skin temperature and pedicel temperature decreased over time (fruit ripening), but a higher drop in temperature was noted when the fruit was stored at 21°C when compared to 13 °C. Vidyarthi et al. (2019) showed that the infrared heating for 25 s

can lead to a sharp temperature rise on the tomato surface, but an insignificant temperature rise in fruit interior. Laguerre et al. (2022) found that the tomato variety and fruit time-temperature change had a significant influence on the evolution of aroma. Furthermore, Kabas et al. (2008) found that the critical height of tomato peel falling damage was 237 mm whereas the maximum contact force and the maximum fruit deformation were 23.81 N and 4.33 mm, respectively. Li et al. (2021) found that the crack propagation in tomato fruit was very sensitive to the tissue failure characteristics, such as failure stress and energy.

To sum up, the existing literature has made great progress in characterizing the heat transfer behavior in tomato fruit or predicting the biomechanical behaviors of tomato fruit by using FE method. Tomato fruit is an irregularly shaped ellipsoid and its internal structure is like a wheel-spoke. Whether the production of tomatoes is carried out in a greenhouse or field, the fruit temperature often changes with the continuous change of the environment temperature (5 ~ 40 °C) throughout the day (Woolf and Ferguson, 2000; Hernandez et al., 2015). However, the biomechanical mechanism of tomato fruit cracking under the coupling effect of environmental temperature field and structural stress field is still unclear. This knowledge gap limits the creation t of effective technical solutions for reducing fruit cracking through environmental temperature control technology in tomato growth management (Hahn, 2011). Taking into account that (1) fruit cracking is accompanied by crack propagation in its internal tissues and that (2) precise experimental quantification of the fruit cracking level (e.g., crack volume) is challenging, the multi-field coupled FE analysis method that can correlate multiple physical fields (such as temperature field and stress field) to solve the nonlinear stress response of a structure under the action of external force (Celik et al., 2011; Fenyvesi et al., 2013) appears very attracting. Moreover, the stronger the sunlight, the faster the temperature around tomato plants rises. In these conditions with increased fruit temperature, there is a high transpiration intensity that results in an increased need for water within cells in the fruit mesocarp tissue, which causes more water absorption and swelling in the corresponding external exocarp and subsequently pericarp cracking (Khadivi-Khub, 2015). This process is similar to a three-point bending test on a rectangular tissue sample (Pitts et al., 2008). Additionally, a mechanical simulation performed on a tissue block rather than the entire fruit can significantly save the computation time while still producing results that are useful and instructive regarding fruit mechanics. Therefore, the purpose of this study is to investigate the biomechanical mechanism of tomato fruit cracking caused by the environmental temperature change using the thermo-biomechanical coupling FE method.

2. Materials and methods

2.1 Investigation of the thermo-biomechanical and heat transfer properties of tomato tissues

Prediction of thermo-biomechanical parameters: The elastic modulus, fracture energy, and failure stress of the exocarp and mesocarp were set as the dependent variables based on the thermo-biomechanical data of the tomato fruit at the light-red ripening stage previously measured by Liu et al. (2022). The temperature was set as the independent variable and six simple linear regression equations (Table 1) were obtained to predict the thermo-biomechanical parameters of tomato exocarp and mesocarp in the temperature range of 5 ~ 41 °C for the following thermo-biomechanical coupling FE model simulation. This temperature range covers the environment temperature change in a greenhouse under sunlight (Hernandez et al., 2015).

Measurement of heat transfer parameters: 60 fresh 'DRK0568' tomatoes at the light-red ripening stage were hand-harvested and then stored in a fridge at 4 °C. As shown in Fig.1A, the measurement method of the thermal conductivity of the tomato exocarp at 5 °C was taken as an example. The first step consists of using a self-developed double-blade cutter to prepare six standards rectangular exocarp tissue samples (length × width: 20 mm × 15 mm) from a tomato fruit freshly removed from the refrigerator. Two samples were randomly taken, clamped to a measuring probe of a thermal conductivity tester (Model: DRE-III, Xiangtan Xiang Instrument Co., Ltd., China) and placed in a climate chamber in which the temperature, relative humidity, and storage time were set 5 °C, 70 %, and 0.5 h, respectively. Both the pre-conditioned samples and the measuring probe as a whole were taken out together from the climate chamber and the output wire in the measuring probe was then immediately connected to the thermal conductivity tester for recording the thermal conductivity of the exocarp at 5 °C. Subsequently, the thermal conductivity measurement of the remaining 2 groups of exocarp tissue samples was performed. Subsequently, the above process was repeated to measure the thermal conductivity of tomato mesocarp tissue at 5 °C. Finally, the same method was used to measure the thermal conductivity of the exocarp and mesocarp samples at 25 °C and 40 °C.

As shown in Fig. 1B, the measurement method in the specific heat capacity of the tomato exocarp was taken as an example. Firstly, 10 ~ 15 g of tomato exocarp tissue samples were prepared using a self-made blade cutter and placed in a vacuum drying oven (Model: DZX-6020B, Shanghai Nanrong Co., Ltd., Shanghai, China) for drying for 3 h at 105 ± 2 °C until its mass remained unchanged (Huang et al., 2016). Subsequently, the dried tomato exocarp tissue samples were ground into powder, and 3.50 mg of the sample was put in a stainless-steel crucible for measuring the specific heat capacity of tomato exocarp tissue using a differential scanning calorimeter (DSC-Q2000, TA Instruments, USA). During measurement, the exocarp powder sample in a

crucible and some sapphire powder as a reference object were set to cool from room temperature (25 °C) to 5 °C, kept for 2 minutes, and then heated from 5 °C to 60 °C at a rate of 5 °C per minute. Three samples were measured and the heat flow - temperature data was recorded in real time. Subsequently, the specific heat capacity of the tomato exocarp tissue at 6 °C, 16 °C, 26 °C, 36 °C, and 46 °C were deduced by the following Eq. (1) (Karthikeyan et al., 2010), respectively. Finally, the same procedure was repeated to measure the specific heat capacity of the tomato mesocarp tissue at 6 °C, 16 °C, 26 °C, 36 °C, and 46 °C.

$$C_p = \frac{m_l}{m_p} \times \frac{DSC_p - DSC_s}{DSC_l - DSC_s} \times C_l \quad (1)$$

The thermal conductivity and specific heat capacity of the tomato exocarp and mesocarp were determined using the heat transfer parameters mentioned above were set as dependent variables whereas the temperature was kept as the independent variable. Four simple linear equations (Table 1) were then regressed to predict the heat transfer parameters of the tomato exocarp and mesocarp in the temperature range of 5 ~ 41 °C for subsequent three-point bending thermo-biomechanical coupling FE simulation.

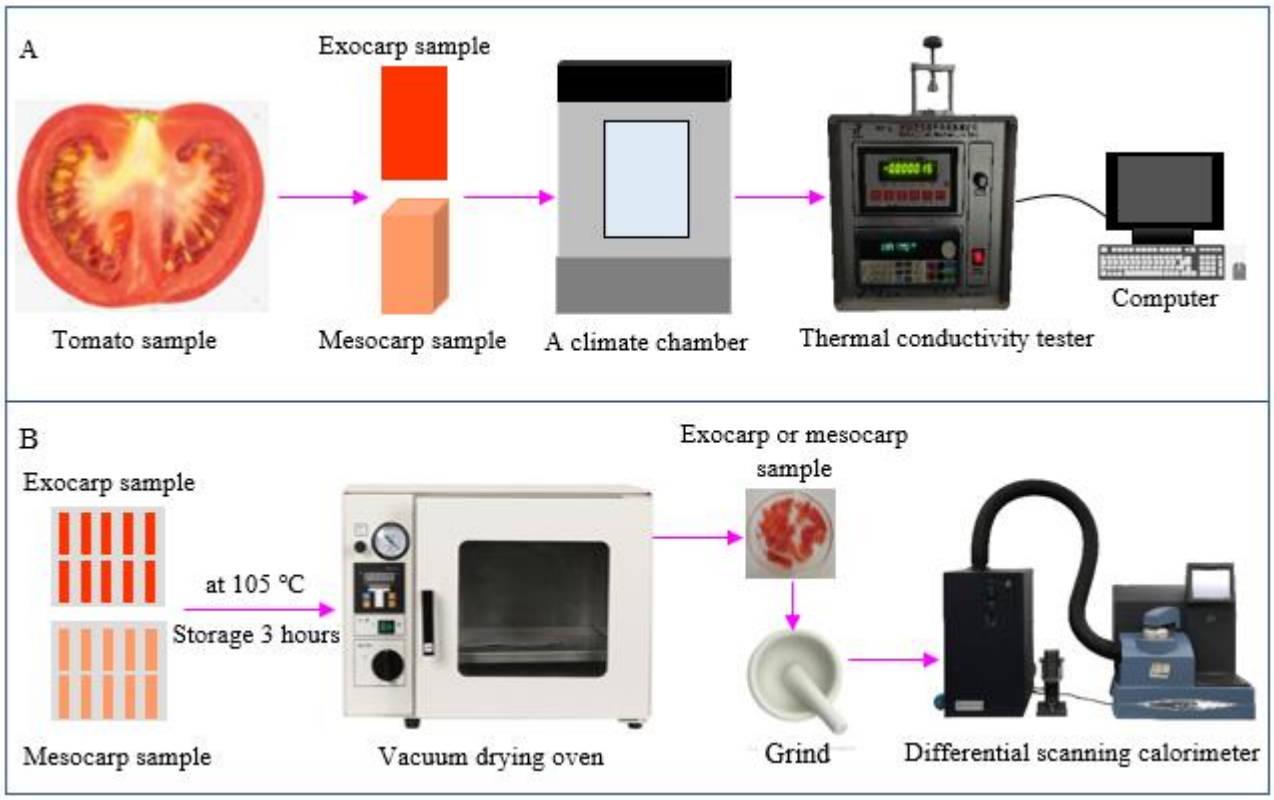

Fig. 1 Measurement of the heat transfer properties of tomato tissues. (A) Measurement process of the tissue thermal conductivity, (B) Measurement process of the tissue heat capacity.

2.2 Thermo-biomechanical coupling three-point bending simulation of tomato pericarp

The thermo-biomechanical coupling with FE simulation for the three-point bending experiment on a

block of tomato pericarp sample during temperature rising was performed by two steps: (1) The heat transfer system in a block of tomato pericarp FE model was established to obtain the temperature profile in the pericarp sample described in Section 2.3.1; (2) A three-point bending FE system was established to combine the obtained temperature profile as an imported predefined temperature field for performing the thermo-biomechanical coupling three-point bending FE simulation, as described in Section 2.3.2.

2.2.1 Simulation of heat transfer in tomato pericarp

2.2.1.1 Heat transfer FE modeling

Geometric modeling: Firstly, the pericarp of a tomato fruit was regarded as a combination of several curved blocks, each pericarp block only contained exocarp and mesocarp tissues, and the thickness of these tissues were measured. Subsequently, a block of tomato pericarp tissue with a curvature radius of 134 mm was geometrically modeled using some operations, such as scanning the contour points, creating spline curves, and extruding (Li et al., 2021) in the Abaqus software (Version 6.20, Dassault Systemes Simulia Corp., USA) (Fig. 2A). In the pericarp model, the exocarp size (arc length × width × thickness) was 46 mm × 8 mm × 0.12 mm and the mesocarp size (arc length × width × thickness) was 46 mm × 8 mm × 4.39 mm.

Definition of the heat transfer analysis step and interaction: In the analysis step, the transient heat transfer analysis method was selected and the time step was set as 5 for simulating the temperature change of the pericarp in greenhouse tomato under sunlight between 9:00 am and 2:00 pm (5 hours). Subsequently, by considering that the elastic modulus of tomato exocarp tissue was higher than that of mesocarp tissue (Li et al., 2021) in the exocarp - mesocarp contact pair, the inner surface of the exocarp model was defined as the master surface and the outer surface of the mesocarp model was defined as the slave surface. The surface - to - surface discretization method was selected to generate the connection coefficients. Two separate surfaces, namely the master and slave surfaces, were connected together by a "Tie" constraint (Fig. 2A), so that the common node had same temperature value on the lower surface of the mesocarp and the upper surface of the exocarp. The position tolerance was defined as the computed default to ensure the nodes from the master surface within which all nodes on the slave surface were tied so that the nodes from the master surface intrigued with all the nodes of the slave surface had the same temperature.

Meshing: Firstly, the exocarp and mesocarp in the pericarp model were relatively regular and both tissues were meshed into eight-node linear heat transfer hexahedral elements DC3D8. Subsequently, in consideration that the element size in the master surface should be larger than that in the slave surface, and the element size

might affect the prediction accuracy and computation time of the FE model (Han et al., 2022), the element size of the exocarp and mesocarp models were set as 0.4 - 0.35 mm, 0.42 - 0.38 mm, 0.45 - 0.4 mm, respectively. Three simple simulations were performed, and it was then found that the setting element size had no significant effect on the accuracy prediction but had a significant effect on the computation time. In order to save computation time and ensure model convergence, in this study, the global sizes of the exocarp and mesocarp were finally set to 0.42 mm and 0.38 mm, respectively, and 1598 and 22896 elements were generated for the exocarp and mesocarp, respectively. The 3D heat transfer FE model of tomato pericarp is shown in Fig. 2B.

Assumption: In this study, several assumptions were given as follows: (i) the tomato exocarp and mesocarp materials are homogeneous and isotropic; (ii) the heat load applying on the tomato exocarp is uniformly distributed, and the heat transfer between adjacent elements in the tomato exocarp and mesocarp occurs only by conduction and follows the heat flux Eq. (2) and the transient heat conduction Eq. (3); (iii) the sunlight radiant heat only transmits to the tomato exocarp surface (i.e. zero penetration depth), and the effect of the heat generated by the respiration of the tomato exocarp and mesocarp tissue on the heat transfer in the tomato pericarp was ignored because the respiration heat in fruit tissue is very low; (iv) the density and Poisson's ratio of the tomato pericarp tissue do not vary with the temperature.

$$q = N \times (-k\Delta T) \tag{2}$$

$$\rho C_p \frac{\vartheta T_p(x,y,z)}{\vartheta t} = -\nabla \times (K\Delta T)_{(x,y,z)} \tag{3}$$

2.2.1.2 Validation of the heat transfer in tomato pericarp

To validate the accuracy of the above developed heat transfer FE model, the simulation and experimental results such as the exocarp surface temperature - time curve, mesocarp center-point temperature - time curve of the heat conduction in elements of the tomato pericarp, with the outer surface subjected to an increasing temperature from 5 °C to 25 °C at a rate of 5 °C per hour, were compared.

Experiment method: Firstly, 30 tomato samples of similar size and shape were selected from the fridge at 4 °C and six points were marked on the equatorial contour of each fruit (Fig. 2C). Subsequently, a fruit sample was taken out from the fridge and its surface temperature was measured using an infrared camera (Model: DM63-S, Dali Technology Co., Ltd., China), and the temperature of mesocarp at the first point with a depth of 4 mm was measured using a thermocouple (Model: WRNK-191, Guan Kuan Co., Ltd., China). Later the remaining 29 fruit samples were measured using the same method, and the recorded average temperature in the exocarp or mesocarp was considered as the initial temperature. All the 30 fruit samples were then put into

189 the climatic chamber at 5 °C with 70% relative humidity for one hour. Subsequently, a fruit sample was taken
190 out from the chamber and its surface temperature and the center-point temperature of the mesocarp at the
191 remaining 5 points were immediately measured using the infrared camera and thermocouple (Fig. 2C and 2D).
192 To ensure the accuracy of the acquired data, the measurement process was conducted within 15 s and six
193 samples were measured one by one at each storage temperature. The average measured temperature in the
194 exocarp or mesocarp was the heat-transferred temperature. Finally, the temperature in the climatic chamber
195 was increased by 5 °C per hour, and the heat-transferred temperatures in the exocarp surface and the center-
196 point of the mesocarp were similarly measured after the fruit samples were stored at 10 °C, 15 °C, 20 °C, and
197 25 °C, respectively. The exocarp surface temperature - time curve, mesocarp center-point temperature - time
198 curve were obtained from the above experimental process.
199 *FE simulation method*: Firstly, the heat transfer parameters (specific heat capacity and thermal
200 conductivity), physical and biomechanical parameters (such as density, Poisson's ratio, elastic modulus) of the
201 exocarp and mesocarp models were defined based on the No.2 in Table 1. The heat transfer and biomechanical
202 parameters of the exocarp and mesocarp tissues at different temperatures were deduced using the
203 corresponding equations in Table 1. Subsequently, the time - temperature load amplitude was applied to the
204 exocarp surface (No.2 in Table 1, Temperature gradient: 5 - 25 °C, $\Delta T_i = 5$); and the initial temperature of the
205 exocarp and mesocarp was defined in the predefined temperature field based on the measured initial
206 temperature value in the above heat transfer experiment. After simulation, the exocarp surface temperature -
207 time curve, and the mesocarp center-point temperature - time curve were extracted during post-processing.
208 **2.2.1.3 Simulation**
209 The temperature in a tomato-growing greenhouse under sunlight radiation always continuously increases from
210 9:00 am to 2:00 pm (Cheng et al., 2021), but the increasing rate could be random (Cheng et al., 2021) because of
211 different factors affecting fruit temperature such as the revolution and rotation of earth, cloud, wind, etc. Hence, the
212 heat transfer FE simulation was designed to two scenarios (Table 1). For the first scenario, it was assumed that from
213 9:00 am to 2:00 pm, the temperature of the exocarp surface increases uniformly every hour. During simulation the
214 temperature gradients and increasing rates were set at three levels: 5 °C - 13 °C, 2 °C per hour; 5 °C - 25 °C, 5 °C
215 per hour; 5 °C - 41 °C, 9 °C per hour. The fruit ripeness was set as two levels: RS_1 and RS_2, and RS_1 refers to the
216 light-red stage while RS_2 refers to a riper stage than RS_1. According to the data of Sirisomboon et al. (2012), the
217 mechanical parameters of tissues at RS_2 were 20% lower than those at RS_1 (Table 1). Furthermore, because some
218 literature showed that the ripeness had no significant effect on the heat transfer parameters of fruit (Correa et al.,

2012; Baptestini et al., 2017), the difference in the heat transfer parameters of the tomato tissues between two ripening stages was ignored here. A total of six simulations (2 ripeness levels × 3 temperature gradient levels) were performed. For the second scenario, it was assumed that from 9:00 am to 2:00 pm the temperature of the exocarp surface increases non-uniformly per hour. During the simulation, the temperature gradients and increasing rates were set as three levels: 5 °C - 13 °C with a continuous increase by 1, 1, 2, and 4 °C every 1 hour within 5 hours; 5 °C - 25 °C with a continuous increase by 2, 4, 6, and 8 °C every 1 hour within 5 hours; 5 °C - 41 °C with a continuous increase by 6, 8, 10 and 12 °C every 1 hour within 5 hours. The ripeness level and its corresponding heat transfer parameters were set as the same as the first scenario. In total, six simulations (2 ripeness levels × 3 temperature gradient levels) were performed. Table 1 shows the simulation design method and parameter settings of the 12 simulations described in this section.

2.2.2 Three-point bending simulation

2.2.2.1 FE modeling of three-point bending loading system

Geometric modeling: Firstly, on the basis of the developed tomato pericarp model, two fixed support points were created on the outer surface of the tomato exocarp to replace the support by the two support plates in the three-point bending experiment, and their distance was 28 mm (Fig. 2E). Subsequently, a 3D discrete rigid-body loading probe geometric model and a 3D rectangular shell plane crack (length × width: 3 × 0.5 mm) were created in Abaqus2020/CAE software for forming a 3D geometric model of three-point bending loading system (Fig. 2E).

Definition of the static mechanics analysis step and interaction: Firstly, the analysis process of the three-point bending system model was defined using the static and general analysis step and the time period was set to 5 subdivided steps corresponding to the pericarp heat transfer model in Section 2.2.1.1. Subsequently, a surface-to-surface contact pair algorithm was defined to the contact interaction between the end-surface (master surface) of the loading probe model and the upper surface (slave surface) of the mesocarp model. The normal contact behavior between the master and slave surfaces follows "hard" contact, and its tangential behavior follows the Coulomb interaction with a friction coefficient of 0.65 (Uba et al., 2020). The interactions between pre-crack and exocarp and pre-crack and mesocarp were defined based on a similar method applied by Liu et al. (2022).

Boundary conditions and meshing: Firstly, two fixed support points were forbidding to translate along the y-axis, while the rigid probe can only allow to move along the y-axis. Afterwards, the pericarp model was re-

meshed for stress analysis, and it requires that (i) the element type should be continuous stress element corresponding to its diffusive heat transfer element in the heat transfer model of Section 2.2.1.1, and (ii) the size and number of the elements in each tissue is same as that in the above heat transfer model. The exocarp and mesocarp were meshed into 8-node hexahedral linear reduced-integration C3D8R elements, and the probe was meshed into 1150 4-node bilinear quadrilateral rigid R3D4 elements with the global size of 0.42 mm. The pre-crack does not require meshing. The extended FE model of the three-point bending system is shown in Fig. 2F.

Assumption: To simplify the following FE simulation, several additional assumptions were as follows: (i) Any physiological changes of pericarp tissue during this simulation were neglected because each three-point bending testing only took about 2 s, considered as very short timescale to cause any significant changes; (ii) the fracture energy (toughness) of fruit tissue is independent of the sample size and the pre-crack size; (iii) the exocarp and mesocarp tissues are linear elastic and ideal brittle solid materials before fracture; (iv) the pre-crack initiation in fruit tissue follows the maximum principal stress criterion in Eq. (4), and the crack evolution follows a linear softening law and a mode-independent and energy-based fracture criterion in Eq. (5).

$$\sigma_{max} \approx \sigma_{max}^{a} \tag{4}$$

$$G \geq G_f \tag{5}$$

2.2.2.2 Validation of the thermo-biomechanical coupling three-point bending FE model

The simulation and experimental results such as the probe loading force - pericarp deflection curve and the crack propagation length in front view - pericarp deflection curve of the three-point bending on the tomato pericarp under the described thermo-biomechanical coupling conditions were compared to confirm the accuracy of the above developed extended FE model.

Experimental method: Firstly, five tomatoes were selected and stored in the climate chamber at 5 °C temperature with 70% relative humidity for one hour. Then, five pericarp samples with the arc length × width × thickness of 46 mm × 8 mm × 4.51 mm were prepared using a self-developed double-blade cutter from a fruit in the climate chamber. A small pre-crack (length × width: 3 × 0.5 mm) was made near the bottom in the middle of radial section using a thin blade according to the National Standard GB / T 7732–2008 (Fig.2G). Subsequently, after each tomato pericarp sample was prepared, it was taken out from the climate chamber immediately and placed on the texture analyzer (Model: Universal TA, Tenge instrument technology Co., Ltd., China) for three-point bending testing (Fig. 2G). The loading displacement was 1.2 mm. Subsequently, the

277 temperature in the climate chamber was increased by 5 °C every hour and, the three-point bending experiments
278 on the pericarp sample stored at 10 °C, 15 °C, 20 °C, or 25 °C were performed, and the corresponding loading
279 displacement was 2.4 mm, 3.6 mm, 4.8 mm, and 6 mm, respectively. During the test, the probe loads the
280 pericarp sample vertically downward from the middle of two support points at a speed of 1 mm/s. The probe
281 loading force - pericarp deflection curve data was recorded in real-time, and the crack propagation length on
282 the front view - pericarp deflection curve was extracted using a similar method to that of Liu et al. (2022). At
283 each storage temperature, five pericarp samples were used to repeat the three-point bending test, and the probe
284 loading force and crack propagation length at each temperature are the mean ± standard deviation for 5 samples.
285 *FE simulation method*: The material properties of the FE model were defined based on the No. 2 in Table
286 1. The maximum principal stress (failure stress) and fracture energy of the exocarp and mesocarp at different
287 temperatures were deduced using the corresponding equations in Table 1. In addition, the temperature solution
288 obtained in Section 2.2.1.2 was imported into the three-point bending FE model as a predefined temperature
289 field instead of the temperature load. A vertically downward displacement load of 6 mm from the loading probe
290 was applied to the midpoint of the pericarp between two support points instead of the force load and the three-
291 point bending simulation was performed. Lastly, the probe loading force - pericarp deflection curve and the
292 crack propagation length - pericarp deflection curve were extracted from the simulation results.

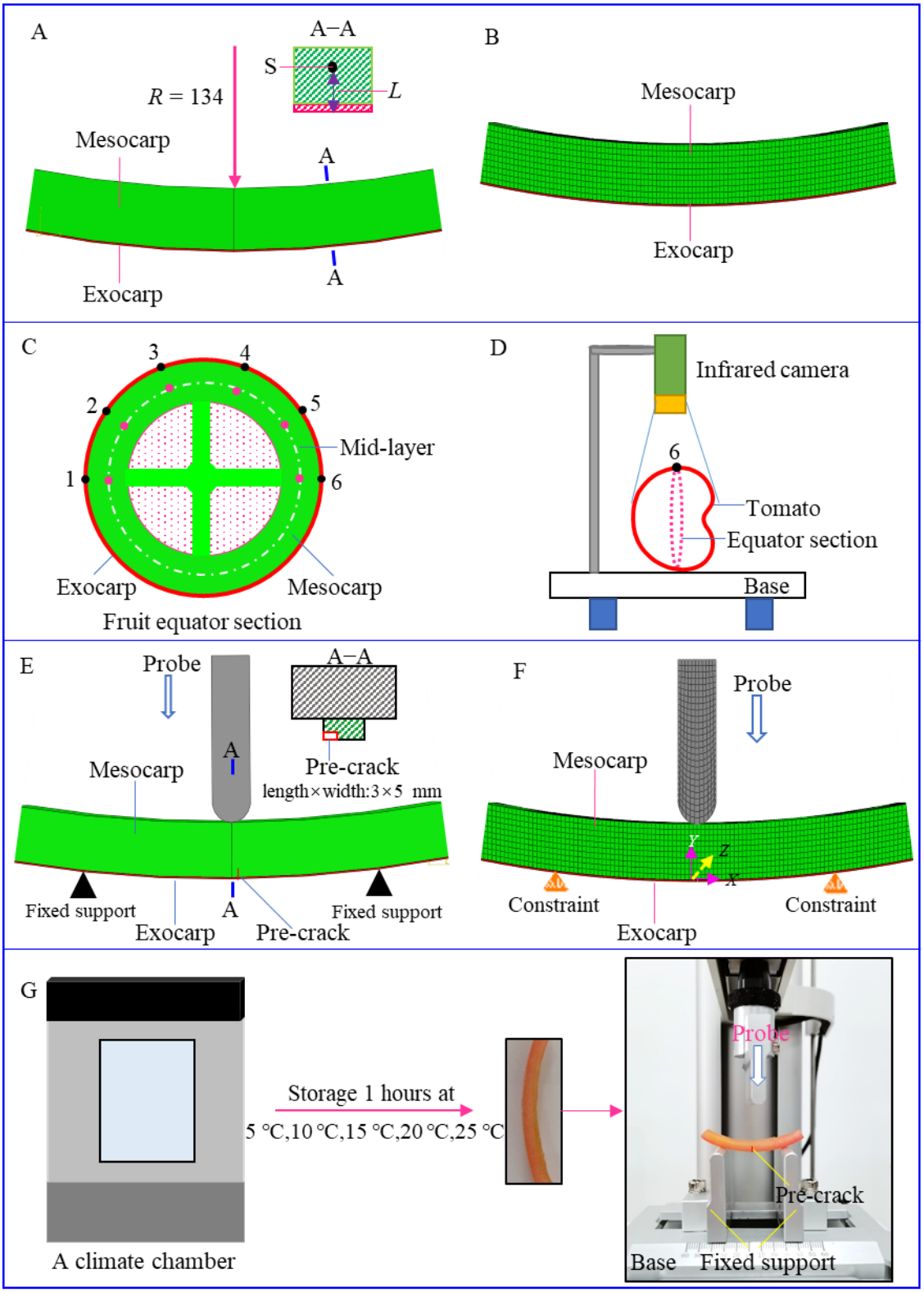

293

294 **Fig. 2** Experiment and simulation of the heat transfer and three-point bending of pericarp. (A) Geometric model
295 of the tomato pericarp, (B) FE model of the tomato pericarp, (C) 12 positions on the fruit equatorial section, (D)
296 Temperature measurement method, (E) Geometric model of three-point bending test system, (F) FE model of
297 three-point bending test system, (G) Three-point bending experiment.

2.2.2.3 Simulation

Corresponding to the Section 2.2.1.3, the simulations were designed in two scenarios (Table 1), namely the temperature of the exocarp surface increases (1) uniformly or (2) non-uniformly per hour. Each temperature solution obtained in Section 2.2.1.3 was imported into the three-point bending FE model as a predefined temperature field instead of the temperature load for simulation in this section. Subsequently, a 6 mm downward displacement load was applied to the midpoint of the pericarp between two support points, and 12 thermo-biomechanical coupling three-point bending FE simulations were then performed.

Table 1 The setting of the heat transfer- and biomechanical parameters in the FE simulations

No. of simulation	Ripening stage	Temperature gradient	Thermo-biomechanical parameters
1	RS_1	5 °C - 13 °C, $\Delta T_i = 2$	$E_{ex} = -0.240\ T + 22.610$, $E_{me} = -0.005\ T + 0.771$
			$\sigma_{maxex} = -0.017\ T + 2.137$, $\sigma_{maxme} = -0.0003\ T + 0.063$
2		5 °C - 25 °C, $\Delta T_i = 5$	$G_{fex} = -0.031\ T + 5.134$, $G_{fme} = -0.010\ T + 2.334$
			$K_{ex} = 0.001\ T + 0.429$, $K_{me} = 0.0005\ T + 0.483$
3		5 °C - 41 °C, $\Delta T_i = 9$	$C_{ex} = 13.52\ T + 4155.9$, $C_{me} = 5.42\ T + 4870.2$
			$\rho_e = 1.01 \times 10^3$, $\rho_m = 0.99 \times 10^3$, $v_{ex} = 0.37$, $v_{me} = 0.35$
4	RS_2	5 °C - 13 °C, $\Delta T_i = 2$	The tissue mechanical parameters at RS_2 was lower 20% than that at RS_1;
5		5 °C - 25 °C, $\Delta T_i = 5$	$K_{ex} = 0.001\ T + 0.429$, $K_{me} = 0.0005\ T + 0.483$
6		5 °C - 41 °C, $\Delta T_i = 9$	$C_{ex} = 13.52\ T + 4155.9$, $C_{me} = 5.42\ T + 4870.2$
			$\rho_e = 1.01 \times 10^3$, $\rho_m = 0.99 \times 10^3$, $v_{ex} = 0.37$, $v_{me} = 0.35$
7	RS_1	5 °C - 13 °C,	$E_{ex} = -0.240\ T + 22.610$, $E_{me} = -0.005\ T + 0.771$
		$\Delta T_1 = \Delta T_2 = 1$, $\Delta T_3 = 2$, $\Delta T_4 = 4$	$\sigma_{maxex} = -0.017\ T + 2.137$, $\sigma_{maxme} = -0.0003\ T + 0.063$
8		5 °C - 25 °C, $\Delta T_1 = 2$,	$G_{fex} = -0.031\ T + 5.134$, $G_{fme} = -0.010\ T + 2.334$
		$\Delta T_2 = 4$, $\Delta T_3 = 6$, $\Delta T_4 = 8$	$K_{ex} = 0.001\ T + 0.429$, $K_{me} = 0.0005\ T + 0.483$
9		5 °C - 41 °C, $\Delta T_1 = 6$,	$C_{ex} = 13.52\ T + 4155.9$, $C_{me} = 5.42\ T + 4870.2$
		$\Delta T_2 = 8$, $\Delta T_3 = 10$, $\Delta T_4 = 12$	$\rho_e = 1.01 \times 10^3$, $\rho_m = 0.99 \times 10^3$, $v_{ex} = 0.37$, $v_{me} = 0.35$
10	RS_2	5 °C - 13 °C,	The tissue mechanical parameters at RS_2 was lower 20% than that at RS_1;
		$\Delta T_1 = \Delta T_2 = 1$, $\Delta T_3 = 2$, $\Delta T_4 = 4$	$K_{ex} = 0.001\ T + 0.429$, $K_{me} = 0.0005\ T + 0.483$
11		5 °C - 25 °C, $\Delta T_1 = 2$,	$C_{ex} = 13.52\ T + 4155.9$, $C_{me} = 5.42\ T + 4870.2$
		$\Delta T_2 = 4$, $\Delta T_3 = 6$, $\Delta T_4 = 8$	$\rho_e = 1.01 \times 10^3$, $\rho_m = 0.99 \times 10^3$, $v_{ex} = 0.37$, $v_{me} = 0.35$
12		5 °C - 41 °C, $\Delta T_1 = 6$,	
		$\Delta T_2 = 8$, $\Delta T_3 = 10$, $\Delta T_4 = 12$	

2.3 Post-processing analysis

For each FE simulation result, the crack propagation length, area, and volume in the exocarp and mesocarp models during the bending test were extracted by the ABAQUS post-processing plug-in Polaris_CrackGeo

program (Star Polaris team, China). The pericarp model consists of the exocarp and mesocarp, so the total crack propagation length in the pericarp model is the sum of the crack propagation lengths in the exocarp and mesocarp models (Eq. 6). Similarly, the total crack propagation area and volume in the pericarp model are the sum of the crack propagation areas and volumes in the exocarp and mesocarp models (Eq. 7 and Eq. 8; Liu et al., 2022), respectively.

$$L_t = \sum_{i=1}^{n} l_{ie} + \sum_{i=1}^{f} l_{im} \tag{6}$$

$$S_c = 2\left(\sum_{i=1}^{k} s_{ie} + \sum_{i=1}^{m} s_{im}\right) \tag{7}$$

$$V_c = \sum_{i=1}^{k} (V_{iexafter} - V_{iexbefor}) + \sum_{i=1}^{m} (V_{imeafter} - V_{imebefor}) \tag{8}$$

2.4 Statistical analysis

The data extracted from the simulation results in No.1 ~ 6 were analyzed by multiple linear regression in SAS software (version 9.2, SAS Institute, Cary, NC, USA) for predicting tomato pericarp cracking susceptibility when the temperature of exocarp surface increased uniformly, and the significance level was set to 0.05 (p = 0.05). Firstly, the temperature gradient, fruit ripeness and pericarp deflection (at the midpoint) were set as independent variables. The temperature gradient having three performance values and the ripeness having two performance values were qualitative variables. Therefore, two dummy variables "ΔT_1" and "ΔT_2" were set for the temperature gradient and "5 - 13 °C", "5 - 25 °C", and "5 - 41 °C" were coded as "00", "01" and "10", respectively; the ripeness stage "RS_1" and "RS_2" were coded as "0" and "1", respectively. The pericarp deflection was a quantitative variable. The crack propagation area and crack propagation volume in the pericarp were defined as dependent variables. The multiple linear regression analyses were then performed by backward elimination method. The data extracted from the simulation results in No.7 ~ 12 were analyzed using the Origin software (Version: 2018, OriginLab Corp., USA) by scatter plots.

3. Results and discussions

3.1 Validation of the tomato pericarp FE model

3.1.1 Validation of the heat transfer in tomato pericarp FE model

Figure 3A shows a final temperature distribution contour in the 3D pericarp heat transfer FE model when the exocarp surface is applied to a temperature load increasing from 5 °C to 25 °C at a rate of 5 °C per hour

(No. 2 in Table 1). An interesting finding was that the temperature distribution in the mesocarp model ranged from 23.5 to 25 °C, while the temperatures on all exocarp elements reached 25 °C. The simulation and experiment results in the exocarp surface temperature - time curve and the mesocarp center-point temperature - time curve are shown in Fig. 3B. Obviously, the temperature on the tomato exocarp surface was slightly higher than that on the center point of the tomato mesocarp. The blue areas were the B-spline error bands of the exocarp surface temperature and the mesocarp center-point temperature during heat transfer experiment for the six tomato fruit samples, respectively. It was obvious that the simulated exocarp surface temperature - time curve and the simulated mesocarp center-point temperature - time curve were within the corresponding error band range. Indeed, the average relative error between the simulation and experimental results in the tomato exocarp surface temperature was about 3.5 ± 1.6 %, and the average relative error between the simulation and experimental results in the temperature of the mesocarp center-point was about 4.6 ± 2.4 %. The error between the values from the simulation and experiment can be attributed to the simplification of the tomato pericarp during the geometrical model or a slight heat loss during the transfer of the sample from the climate chamber to their infrared temperature measurement location. The above two results showed that the average relative error between the simulation and experimental data was below 5 % (Fig. 3B). Hence, the FE model has a high prediction accuracy and could be used in the following research on the heat transfer sensitivity analysis.

3.1.2 Validation of the thermo-biomechanical coupling three-point bending FE model

Figure 3C shows the final crack propagation state and Von mises stress distribution of a thermo-biomechanical coupling pericarp FE model when a downward displacement load of 6 mm was applied above the midpoint of the pericarp between the two support points. The von Mises stresses in the exocarp and mesocarp models varied from 0 to 1.7 MPa and 0 to 0.3 MPa, respectively. Fig. 3D is the experimental result corresponding to Fig. 3C. Whether in the simulation or experimental results, the pre-crack in the pericarp under displacement loading simultaneously propagated along arbitrary elements in the *y*- and *z*-axis directions of the exocarp and mesocarp, forming two uneven crack surfaces in 3D space. The crack propagation state between the simulation and experiment was similar (Fig. 3C and 3D).

Figures 3E and 3F show the experiment and simulation results of the three-point bending test on the pericarp model when the exocarp surface was subjected to a temperature load increasing from 5 °C to 25 °C at a rate of 5 °C per hour. It was found that there was a nonlinear positive correlation between the probe loading

force and pericarp deflection extracted from the simulation and experimental results in the thermo-biomechanical coupling three-point bending model (Fig. 3E). The blue area is a B-spline error band with the probe loading force varied with the pericarp deflection increase during the three-point bending experiment for the five investigated pericarp samples. Obviously, the simulated probe loading force - pericarp deflection curve was within the error band range (Fig. 3E). When the deflection of the tomato pericarp sample increases from 0 to 6 mm, the probe loading force in the thermo-biomechanical coupling three-point bending simulation process increases from 0 to 0.68 N, whereas the average probes loading force of the five pericarp samples undergoing the three-point bending experiment increases from 0 to 0.66 N. The average relative error between the simulation results and the experimental results was 3.0 ± 2.3 %. As shown in Fig. 3F, there was an approximate nonlinear positive correlation between the crack propagation length and pericarp deflection extracted from the simulation and experimental results. The blue area is the B-spline error band of the average crack propagation length varied with the increased pericarp deflection on the front view of the pericarp sample during three-point bending experiment for five pericarp samples. It is apparent that the simulated crack propagation length - pericarp deflection curve on the front view of the pericarp sample was within the error band (Fig. 3F). The crack in the front view in the simulation process of the three-point bending pericarp model expanded from 0.5 to 2.58 mm when a vertical downward displacement of 6 mm was applied on the pericarp sample. During the experiment, the crack propagation of the pre-cracks in the front view of the five pericarp samples increased from 0.5 to 2.64 mm, and the average relative error between the simulation and experiment results was 4.3 ± 2.3 %.

To sum up, the final crack propagation state in the pericarp, the probe loading force - pericarp deflection curve, and the crack propagation length - pericarp deflection curve of the three-point bending experiment approximated the simulation result values. Therefore, the established FE model had a high prediction accuracy, and could be used in the following prediction of the tomato pericarp cracking susceptibility.

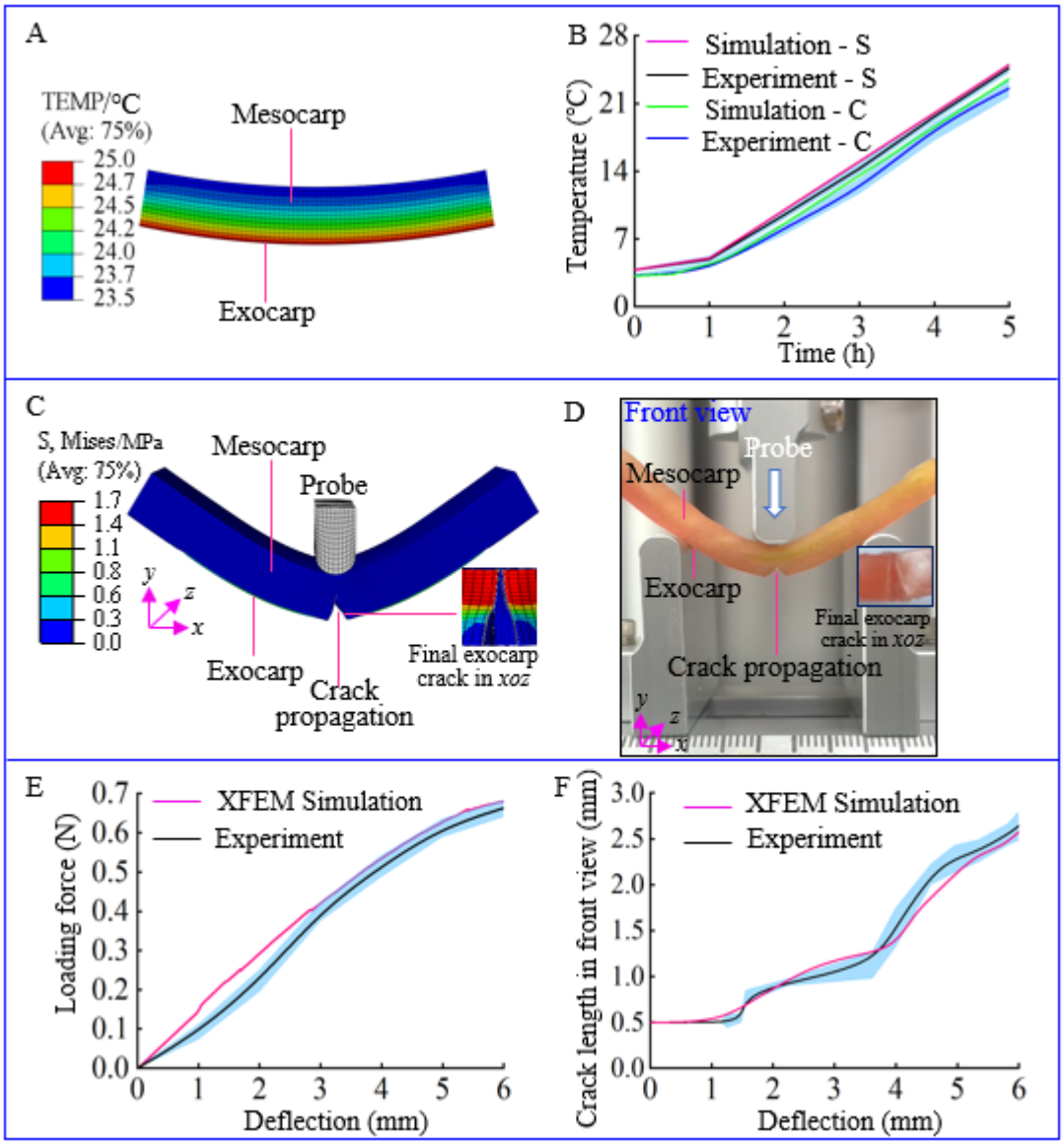

Fig. 3 Validation of the heat transfer FE model and the three-point bending FE model. (A) Temperature distribution contour of pericarp; (B) Temperature - time curves in the heat transfer experiment and simulation, the blue area is the B-spline error band (Mean ± Standard deviation) of experiment result, Simulation - S and Experiment - S represent the exocarp surface temperature in simulation and experiment, Simulation - C and Experiment - C represent the mesocarp center-point temperature in simulation and experiment; (C) Final crack status and Von Mises stress distribution; (D) Crack propagation in front view; (E) Probe loading force - deflection curves in the experiment and XFEM simulation, the blue area is the B-spline error band (Mean ± Standard deviation) of the experiment results; (F) Crack length on front view - deflection curves in experiment and XFEM simulation, the blue area is the B-spline error band (Mean ± Standard deviation) of the experiment results.

3.2 Sensitivity of the heat transfer and three-point bending FE model to temperature and ripening stage

3.2.1 Sensitivity of the heat transfer and three-point bending FE model to fruit temperature

Figure 4-A1 shows the exocarp surface temperature - time curve under three temperature gradient levels when the tomato exocarp surface temperature uniformly increases. Obviously, the exocarp surface temperature under each temperature gradient completely reached the set surface temperature value. Figure 4-A2 shows the temperature - time curve at the center-point of the tomato mesocarp obtained from the simulation of pericarp heat transfer under three temperature gradients when the surface temperature of the tomato pericarp increased uniformly. It was found that the heat transfer rates in the pericarp tissue model under three temperature gradients were 1.99, 4.78, and 8.50, respectively. Noticeably, there was a linear (uniform) positive correlation between the mesocarp center-point temperature and time. Moreover, the greater the temperature gradient on the exocarp surface the higher was the temperature on the mesocarp center-point with the increase of heat transfer time. These results indicated that, with the increase of sunlight radiation time (Vidyarthi et al., 2019), the tomato fruit surface in the greenhouse absorbs more heat, and the heat transfer rate in the pericarp tissue is faster and the mesocarp center-point has a greater temperature.

Figures 4-B1, B2, and B3 show the probe loading force - pericarp deflection curve, pericarp crack propagation area - pericarp deflection curve, and crack propagation volume - pericarp deflection curve in the thermo-biomechanical coupling three-point bending FE simulation under three temperature gradients when the temperature applied to the tomato exocarp surface uniformly increased. In the thermo-biomechanical coupling three-point bending simulation, the deflection deformation at the middle position of the pericarp sample showed a linear and then nonlinear increase trend with the increase of the probe loading force (Fig. 4-B1). When the probe loading force was less than 0.4 N, no obvious influence by the temperature gradients of the exocarp surface on the probe loading force - pericarp deflection behavior could be observed. When the probe loading force was greater than 0.4 N, a clear influence by the temperature gradients of the exocarp surface on the probe loading force - pericarp deflection behavior could be observed. The pericarp deflection deformation increased with increasing temperature gradient. When the probe loading force of the thermo-biomechanical coupling three-point bending model was 0.5 N, the pericarp deflections of the pericarp model at the temperature gradient of 5 - 41 °C were 1.07 and 1.15 times more than those of 5 - 25 °C and 5 - 13 °C, respectively. In the thermo-biomechanical coupling three-point bending simulation, the crack propagation area and crack propagation volume on the pericarp model showed a nonlinear increase trend from slow to fast with the increase of deflection deformation at the midpoint of the pericarp (Fig. 4-B2 and B3). The temperature gradients of the exocarp surface had a gradual apparent influence on the crack propagation area and volume of the pericarp XFEM model with the increased deflection deformation in the middle of the pericarp. The larger

the temperature gradient on the exocarp surface, the smaller the crack propagation area and volume of the pericarp model. When the deflection in the middle of the pericarp of the thermo-biomechanical coupling three-point bending model was 6 mm, the crack propagation area and volume of the pericarp of the three-point bending thermo-biomechanical coupling model at the temperature gradient of 5 - 13 °C were 1.28 and 1.72, 1.19 and 1.49 times more than that at the temperature gradient of 5 - 25 °C and 5 - 41 °C, respectively. The reason behind this might be that there was obvious difference in the elastic modulus of the pericarp at different temperatures. The lower the temperature of any pericarp element, the greater the elastic modulus of the pericarp (Khanal, 2017). This resulted in a faster crack propagation speed on the XFEM models. Therefore, under the same pericarp deflection, smaller temperature gradient induces larger final crack propagation area and volume. This result indicated that the temperature gradient on the tomato exocarp surface has an important effect on the tomato pericarp cracking susceptibility. Sunlight causes a rise in the fruit exocarp surface temperature, which also intensifies the plant transpiration process, water absorption in the mesocarp and swelling. This results in an increased pressure on the exocarp exerted by the tomato mesocarp, causing a higher intercellular porosity, thereby reducing the hardness and strength of the tomato pericarp and weakening the anti-cracking ability of the tomato pericarp (Khadivi-Khub, 2015). Therefore, a larger temperature gradient on the tomato exocarp surface results in a greater deflection deformation in the middle of the pericarp XFEM model, which increases the cracking susceptibility of the tomato pericarp.

3.2.2 Sensitivity of the heat transfer and three-point bending FE model to fruit ripening stage

Figure 4-C1 shows the center-point temperature - time curve at two ripening stages under the same temperature gradient conditions. Figures 4-D1, D2, and D3 show the probe loading force - pericarp deflection curve, pericarp crack propagation area - pericarp deflection curve, and crack propagation volume - pericarp deflection curve in the thermo-biomechanical coupling three-point bending FE simulation at two ripeness stages under the same temperature gradient, respectively. In the thermo-biomechanical coupling three-point bending simulation, the deflection of the pericarp central axis shows a nonlinear increase trend with the increased probe loading force (Fig. 4-D1). The ripeness stages of the tomato fruit had a gradual obvious influence on the deflection deformation at the pericarp middle position of the thermo-biomechanical coupling three-point bending model with the increase in the probe loading force. Moreover, the higher ripening stage of tomato fruit resulted in a smaller deflection deformation in the pericarp model. When the probe loading force of the thermo-biomechanical coupling three-point bending model was 0.5 N, the pericarp deflection at RS_1 was

1.34 times more than that at RS_2, which may be attributed to the significant differences in biomechanical parameters, such as elastic modulus of pericarp at different ripeness stages. The higher the ripening period of tomato fruit is, the smaller the elastic modulus and stiffness of tomato pericarp are (Matas et al., 2005), and the easier it is to deform under the same probe loading force. The pericarp crack propagation area and crack propagation volume show a nonlinear increase trend with increased pericarp deflection (Fig. 4- D2 and D3). When the deflection in the middle of the pericarp of the three-point bending thermo-biomechanical coupling model was 6 mm, the pericarp crack propagation area and volume at the ripening stage of RS_1 were 1.15 times and 1.48 times more than those at RS_2, respectively. The observed trend may be explained by the fact that higher elastic modulus of the pericarp results in faster crack propagation speed on the XFEM model. Indeed, under the same deflection deformation, a lower ripeness of the tomato fruit resulted in a faster crack propagation speed and larger final crack propagation area and volume (Li et al., 2021; Liu et al., 2022). Therefore, the effect of ripeness on the elastic modulus of the tomato pericarp directly affects the cracking sensitivity of the tomato pericarp. Indeed, higher ripeness level of the tomato fruit makes the fruit less resistance to crack.

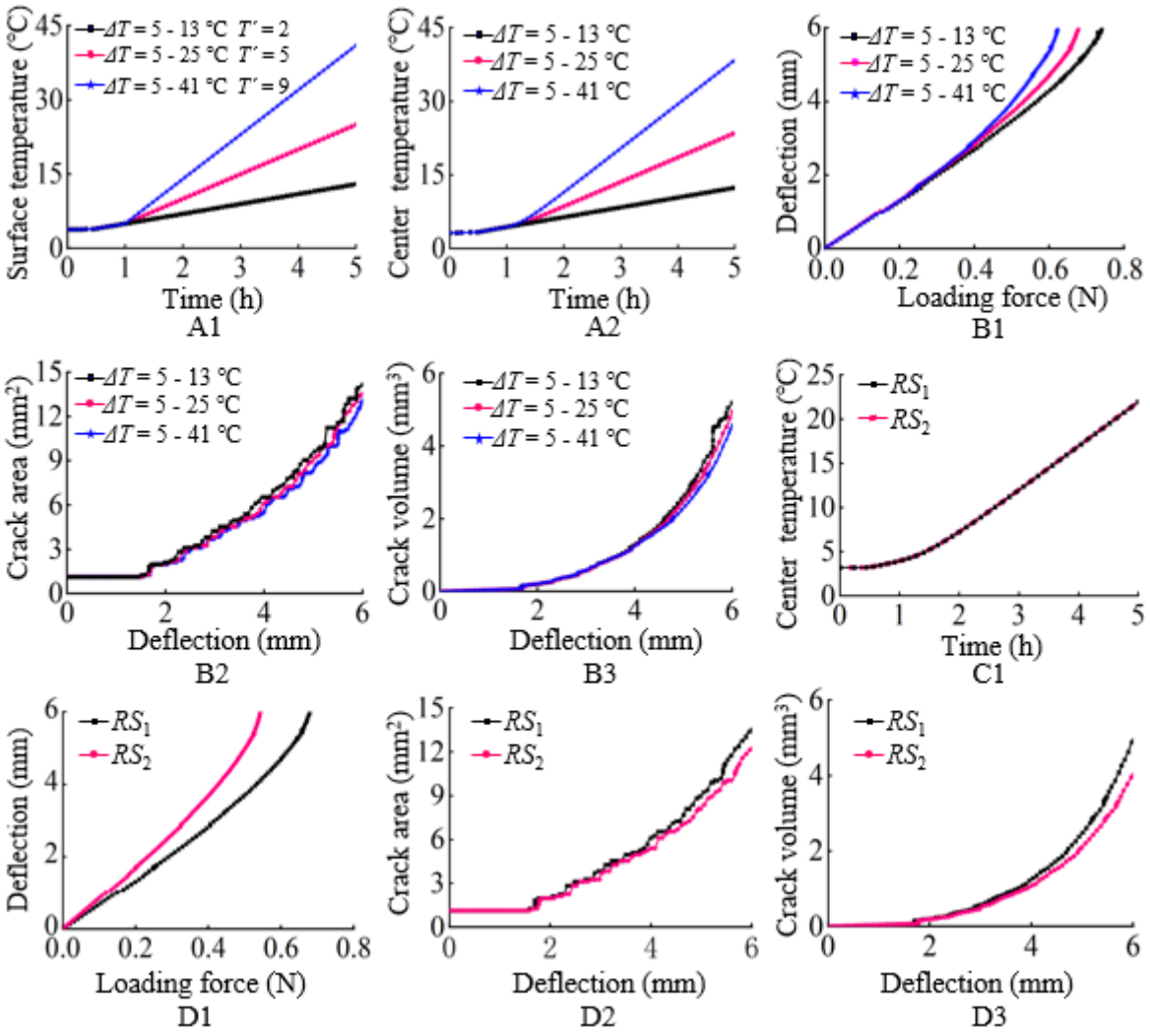

Fig. 4 Sensitivity analysis of the heat transfer FE model and the three-point bending FE model. (A1, A2) Sensitivity of the heat transfer FE model to temperature, (B1, B2, B3) Sensitivity of the three-point bending FE model to temperature, (C1) Sensitivity of the heat transfer FE model to fruit ripening stage, (D1, D2, D3) Sensitivity of the three-point bending FE model to fruit ripening stage.

3.3 Prediction of the cracking susceptibility of tomato pericarp

3.3.1 Prediction of the cracking susceptibility of the tomato pericarp under a uniform increase in temperature

Eqs. (9 - 11) show the multiple linear regression mathematical models with the loading peak force, pericarp crack propagation area, and crack propagation volume as dependent variables, respectively. The results of multiple linear regression analysis showed that when there was a uniform increase in temperature on the tomato exocarp surface, three independent variables: temperature gradient, fruit ripeness, and pericarp

deflection (at the midpoint) had significant effects on three dependent variables: loading peak force, pericarp crack propagation area, and crack propagation volume ($p < 0.05$). In descending order, the factors affecting the cracking susceptibility of the tomato pericarp include pericarp deflection, ripeness stage, and temperature gradient. In the three-point bending simulation, when the pericarp deflection increased by 1 mm, the loading peak force, crack propagation area, and crack propagation volume increased by 0.09 N, 1.03 mm^2, and 2.60 mm^3, respectively. In the three-point bending thermo-biomechanical coupling simulation, the peak load force, crack propagation area and crack propagation volume at the RS_1 ripening stage was 0.08 N, 0.62 mm^2, and 1.18 mm^3 higher than those at the RS_2 ripening stage, respectively. When the temperature gradient was "5 - 13 °C", the peak load, crack propagation area, and crack propagation volume of pericarp were the largest, which were 0.03 N, 0.26 mm^2, and 0.56 mm^3 higher than those at the temperature gradient of "5 - 25 °C". When the temperature gradient was "5 - 41 °C", the load peak force, crack propagation area, and crack propagation volume of pericarp were the smallest, which were 0.03 N, 0.32 mm^2, and 0.60 mm^3 smaller than those at "5 - 25 °C", respectively.

The greater the temperature gradient applied to the tomato exocarp surface, the greater was the temperature gradient on the tomato mesocarp center-point after heat transfer and the smaller was the peak load force required for the pericarp cracking. A temperature gradient on the exocarp surface always exists during tomato development, because of the temperature difference in a certain area of the tomato fruit surface from morning to noon under the sunlight radiation or the temperature difference between the sun-exposed surface and the shaded surface in a fruit. Therefore, when the environment temperature difference between noon and morning is large, the tomato fruit is more likely to crack. At the same initial temperature, when the temperature on the sun-exposed fruit surface increased faster than that on shaded air temperature, the temperature gradient of the pericarp on the sun-exposed fruit surface was greater than that on the shaded air temperature, and the fruit on the sun-exposed fruit surface was more prone to crack. These results of a higher cracking rate of the tomato pericarp with the increased temperature gradient corroborate with the experimental results of De Oliveira et al. (2015) for a tomato peel, Koumanov (2015) Cherry peel, El-Rhman (2010) pomegranate peel, and Li et al. (2022) for a navel orange peel. These findings are understandable because when the temperature gradient of the plant growth environment caused by light is large, the water absorption rate and transpiration of the fruit increase. Therefore, the fruit absorbs more water, expands, and the accumulation rate of soluble solids in the fruit accelerates. These processes, directly increase the pressure exerted by the tomato mesocarp on the exocarp, and thus affect its cracking rate (Correia et al., 2018; Singhet al., 2020; Li et al., 2021). During

515 the warming process, both exocarp and mesocarp tissues swell with heat transfer from the exocarp to mesocarp,
516 but the difference in swelling degree between exocarp and mesocarp tissue cells also affects the fruit cracking
517 rate (khadivi khub, 2015; Correia et al., 2018; Mustafa et al., 2019). In addition, intense light may also burn
518 the pericarp and damage the integrity of the pericarp and cuticle, which is one of the reasons for the increasing
519 probability of fruit cracking (Li and Chen, 2017). Therefore, it is effective to reduce the cracking rate by timely
520 shading the tomato fruit during growth to regulate the greenhouse sunlight intensity and the environmental
521 temperature gradient of the fruit.

522 The effect of ripening stage on the cracking susceptibility for the tomato pericarp is similar to that reported
523 for other fruit systems, such as nectarine peel (Gilbert et al., 2007), tomato peel (Dominguez et al. , 2012),
524 jujube peel (Li et al., 2019), and litchi peel (Fahima et al., 2019). That is, the cracking rate of the fruit is
525 significantly positively correlated with the ripening stage and the higher the fruit degree of ripeness, the smaller
526 is the peak load force required for peel cracking, and the easier the fruit is to crack. This could be attributed to
527 the difference in the contents of protopectin, cellulose, hemicellulose, boron, and calcium ions in the pericarp
528 of fruits at different ripeness stages (Khadivi-Khub, 2015; Li and Chen, 2017; Mustafa et al., 2019), resulting
529 in different elastic-plastic biomechanical characteristics (such as elastic modulus, fracture stress and strain) of
530 the pericarp or epidermis (Bargel and Neinhuis, 2005; Sirisomboon et al., 2012), thus affecting the cracking
531 susceptibility of fruits.

532 In this study, a thermo-biomechanical coupling three-point bending test was conducted to simulate the
533 cracking of the tomato pericarp induced by the increase of internal swelling pressure by applying displacement
534 load (i.e. loading deflection) from inside to outside under a greenhouse environment. Research shows that
535 greater load deflection increases the likelihood of the fruit pericarp to crack; that is, the greater the fruit
536 swelling pressure, the more likely is the fruit to crack (Koumanov, 2015; Bruggenwirth and Knoche, 2017；
537 Schumann and Knoche, 2020). Similarly, the larger the load deflection, the larger the pericarp crack
538 propagation area and volume. Thus the greater the fruit swelling pressure, the greater the final size of the
539 pericarp crack. This could be explained by the fact that when the internal swelling pressure of tomato mesocarp
540 cells continues to increase, the corresponding external exocarp is tensed, which easily results in pericarp
541 cracking (Khadivi-Khub, 2015; Liu et al., 2022). The cell swelling pressure of fruit is related to the water
542 absorption rate of the fruit, and the size of the induced water potential and hydraulic conductivity during fruit
543 growth are the main factors affecting the location and extension of fruit cracking (Hossain and Nonami, 2012;
544 Khadivi-Khub, 2015). These results have shown that different irrigation methods should be adopted according

to the weather conditions and the water demand for fruit during growth to effectively reduce the fruit cracking rate.

$$F = 0.09\ L_d - 0.06\ T_1 - 0.03\ T_2 - 0.08\ RS + 0.18 \quad (9)$$

$$S_c = 1.03\ L_d - 0.58\ T_1 - 0.26\ T_2 - 0.62\ RS - 1.71 \quad (10)$$

$$V_c = 2.60\ L_d - 1.16\ T_1 - 0.56\ T_2 - 1.18\ RS - 3.49 \quad (11)$$

3.3.2 Prediction of the cracking susceptibility of the tomato pericarp under a non-uniform increase in temperature

Figure 5A shows the heat transfer effect of the tomato pericarp when the temperature of its surface increases at a non-uniform rate. Obviously, the mesocarp center-point temperature increased with the non-linear (non-uniform) increasing exocarp surface temperature. Figure 5B shows the deflection deformation of the tomato pericarp when the temperature its surface increases at a non-uniform rate. Indeed, the variation in the pericarp's deflection deformation among different non-uniform temperature gradient levels in the thermo-biomechanical coupling three-point bending FE model became increasingly apparent with an increase in the probe loading force. Under the same loading force, the pericarp deflection was positively correlated with the hourly tomato pericarp surface temperature. These findings also suggest that a larger hourly temperature increase in the tomato pericarp surface would result in less resistance of the fruit to surface cracking. This is presumably attributed to the decrease in the elastic modulus of pericarp tissue because of the direct relationship between the hourly rising temperature with the increasing temperature of the tomato pericarp components (Li et al., 2021). Therefore, under the same probe loading force, the ability of the pericarp to resist cell expansion and rupture is weakened and the fruit easily cracks at higher rate of temperature increase. Figures 5C and 5D show the crack propagation area and crack propagation volume in tomato pericarp FE model when the temperature of tomato exocarp surface increase at a non-uniform rate. Obviously, the crack propagation area and crack propagation volume in pericarp showed a nonlinear increasing trend with the increased pericarp deflection. Similar to the findings by Li et al. (2021) on tomato pericarp cracking, for the same loading deflection, the higher the hourly increasing temperature on the pericarp surface, the smaller the crack propagation area and crack propagation volume. As previously mentioned, the pericarp elastic modulus decreases with increasing hourly temperature, which causes a slower pericarp crack propagation speed on the XFEM model and a smaller ultimate fracture propagation area and volume under the same loading deflection.

In this section, the effect of the non-uniform temperature increase rate on the tomato exocarp surface at

574 the temperature gradient of 5 - 25 °C on the heat transfer, deflection deformation, and crack propagation of the
575 pericarp was taken as an example to compare with the above-mentioned uniform increased rate of the
576 temperature conditions. The results of the heat transfer simulation showed that when the heat transfer time was
577 5 h, the mesocarp center-point temperature was slightly lower than the exocarp temperature. The mesocarp
578 center-point temperature under the non-uniform temperature increasing rate was 0.86 times lower than that
579 under the uniform temperature increasing rate. Furthermore, in the thermo-biomechanical coupling three-point
580 bending FE model, when the probe loading force was 0.6 N, the pericarp deflection at the non-uniform
581 temperature increasing rate was 0.95 times that at the uniform temperature increasing rate, and the latter was
582 easier to crack than the former. When the pericarp deflection was 6 mm, the crack propagation area and volume
583 of the pericarp under non-uniform temperature increasing rate were 1.01 and 1.02 times than those under the
584 uniform temperature increasing rate, respectively. This suggests that the temperature of the pericarp elements
585 under the non-uniform temperature increasing rate is lower than that under the uniform temperature increasing
586 rate. Under the same probe loading force, the pericarp deflection deformation is large and the tomato pericarp
587 is easy to crack under the uniform temperature increasing rate applied to the exocarp surface. This could be
588 explained by the difference in chemical and physiological responses of the tomato pericarp tissue materials
589 affected by uniform and non-uniform temperature increasing rate, which leads to different elastic-plastic
590 biomechanical behaviors. Non-uniform temperature increasing rate may affect fruit growth rate and
591 physiological performance (Chen et al., 2017; Wu et al., 2017; Reich et al., 2018). Plant physiological behavior
592 is highly sensitive to temperature changes (He et al., 2020). These results provide substantial evidence that in
593 the growing season, the non-uniform and rapid increase in daytime temperature tends to inhibit the growth of
594 vegetation (Wang et al., 2009). An environmental temperature of fruit growth with an appropriate non-uniform
595 temperature increasing rate could help to reduce the cracking rate of fruit.

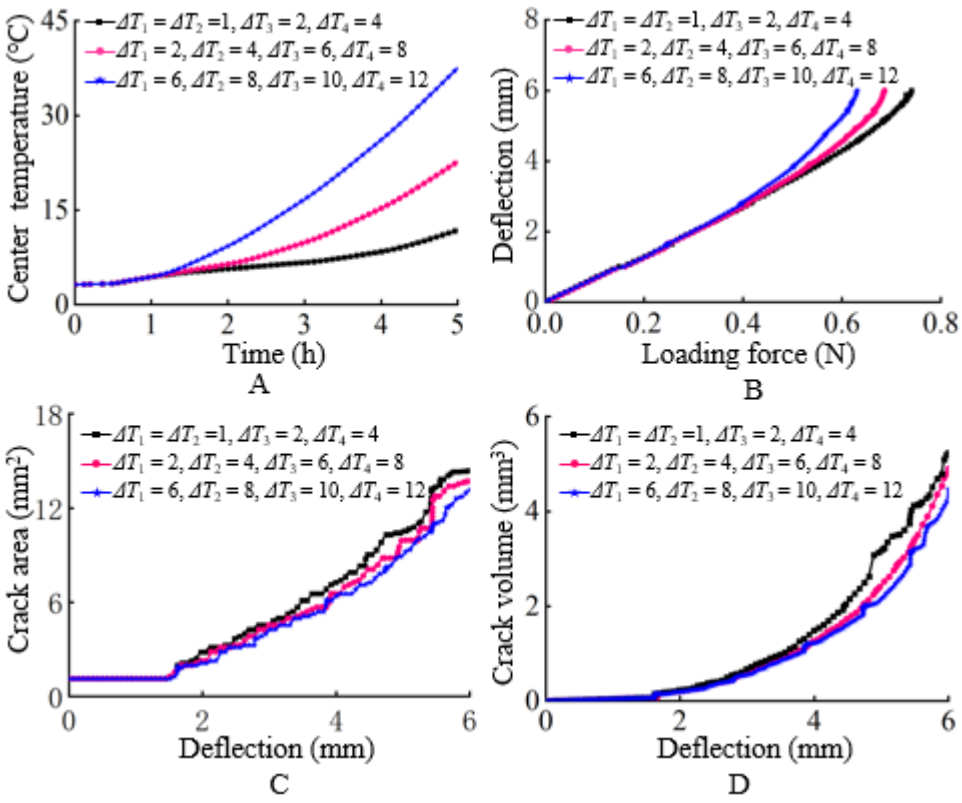

Fig. 5 Heat transfer, deflection and crack propagation of the tomato pericarp under a non-uniform increase in the temperature. (A) Heat transfer in the pericarp, (B) Loading force *vs* pericarp deflection curve, (C) Pericarp deflection *vs* crack area curve, (D) Pericarp deflection *vs* crack volume curve.

4. Conclusion

The cracking susceptibility of tomato pericarp subjecting to uniform and non-uniform temperature increasing rate at different ripening stages were investigated by the thermo-biomechanical coupling three-point bending FE simulation and validated with experiments using a texture analyzer. The results showed that the FE model of tomato pericarp is capable of reproducing the experimental probe loading force - pericarp deflection curve and the crack propagation length - pericarp deflection curve in deflection deformation up to 6 mm. Although there was no obvious difference between the two fruit ripeness stages when the temperature of the tomato exocarp surface increased uniformly, the temperature in the center of the tomato pericarp depended clearly on the temperature gradient in the exocarp surface. As the pericarp deflection increased, the crack propagation area and volume in the pericarp FE model became gradually more sensitive to the temperature gradient and fruit ripeness stage. Three mathematical models were found to have the ability to quantitatively predict the cracking susceptibility of tomato pericarp at two ripening stages under different environmental temperature gradients. The results showed that the pericarp deflection was the most significant factor affecting the cracking susceptibility of the pericarp,

followed by the ripeness stage and temperature gradient. Furthermore, the temperature at the center point of the mesocarp subjected to a non-uniform temperature increase was slightly lower than that from a uniform increase in the temperature, which indicated that the tomato pericarp has a better anti-cracking ability when its surface was subjected to a non-uniform temperature increase rate when compared to conditions with a uniform rate of increase in the temperature. If the temperature gradient applied on the exocarp surface reflects the difference between the temperature of the sun-exposed and shaded fruit surfaces, it is further illustrated that the high temperature difference between two fruit surfaces increases the cracking susceptibility of fruit. This study provides a valuable method for reducing fruit cracking by controlling different greenhouse environment (sunlight and temperature) at different ripening stages and thus contributes to fruit waste reduction and fruits economics improvement. This emerging thermo-biomechanical coupling extended-FE technology can also be applied to other fresh fruits for improving their economics of production while reducing waste.

Acknowledgements

This work was supported by a European Marie Curie International Incoming Fellowship (326847 and 912847), a Chinese Universities Scientific Fund (2452018313), and a Project of the Key Laboratory of Equipment and Informatization in Environment Controlled Agriculture (Ministry of Agriculture and Rural Affairs) of Zhejiang University (2011NYZD2004).

Author contributions

Huijie Liu: Conceptualization, Methodology, Investigation, Data curation, Writing – original draft. Zhiguo Li and Jianping Li: Conceptualization, Investigation, Writing – review & editing, Supervision. Pengfei Zhu: Data curation, Writing – original draft. Fideline Tchuenbou-Magaia: Writing – review & editing, Supervision. Jiheng Ni: Writing – review & editing, Supervision.

634 **References**

635 Bargel, H., Neinhuis, C., 2005. Tomato (*Lycopersicon esculentum Mill*) fruit growth and ripening as related to
636 the biomechanical properties of fruit skin and isolated cuticle. J. Exp. Bot. 56, 1049-1060.
637 https://doi.org/2005;56:1049-60. 10.1093/jxb/eri098.

638 Baptestini, F.M., Corrêa, P.C., Oliveira, G.H.H.D., Botelho, F.M., Oliveira, A.P.L.R., 2017. Heat and mass
639 transfer coefficients and modeling of infrared drying of banana slices. Revista Ceres. 64, 457-464.
640 https://doi.org/10.1590/0034-737x201764050002.

641 Bruggenwirth, M., Knoche, M., 2017. Cell wall swelling, fracture mode, and the mechanical properties of
642 cherry fruit skins are closely related. PLANTA. 245, 765-777. https://doi.org/10.1007/s00425-016-2639-
643 7.

644 Celik, H.K., Rennie, A.E.W., Akinci, I., 2011. Deformation behaviour simulation of an apple under drop case
645 by finite element method. J. Food Eng. 104, 293-298. https://doi.org/10.1016/j.jfoodeng.2010.12.020.

646 Chen, C., Zhang, D., Li, P., Ma, F., 2012. Partitioning of absorbed light energy differed between the sun-
647 exposed side and the shaded side of apple fruits under high light conditions. Plant Physiol. Biochem. 60,
648 12-17. https://doi.org/10.1016/j.plaphy.2012.07.016.

649 Correa, P.C., De Oliveira, G.H.H., Baptestini, F.M., Diniz, M., Da Paixao, A., 2012. Tomato infrared
650 drying:modeling and some coefficients of the dehydration proccess. Chil. J. Agric. Res. 72, 262-267.
651 https://doi.org/10.4067/S0718-58392012000200015.

652 Chen, B.M., Gao, Y., Liao, H.X., Peng, S.L., 2017. Differential responses of invasive and native plants to
653 warming with simulated changes in diurnal temperature ranges. Aob Plants. 9, plx028. https://doi.org/
654 10.1093/aobpla/plx028.

655 Correia, S., Schouten, R., Silva, A.P., Goncalves, B., 2018. Sweet cherry fruit cracking mechanisms and
656 prevention strategies: A review. Sci. Hortic. 240, 369-377. https://doi.org/10.1016/j.scienta.2018.06.042.

657 Cheng, W., He, J.L., Liu, Z.H., 2021. Evaluating how the temperature changes in a sunken solar greenhous.
658 Eng. Agric. 41, 279-285. https://doi.org/10.1590/1809-4430-Eng.Agric.v41n3p279-285/2021.

659 Dominguez, E., Fernandez, M.D., Hernandez, J.C.L., Parra, J.P., Espana, L., Heredia, A., Cuartero, J., 2012.
660 Tomato fruit continues growing while ripening, affecting cuticle properties and cracking. Physiol. Plant.
661 146, 473-486. https://doi.org/10.1111/j.1399-3054.2012.01647.x.

662 De Oliveira, G.H.H., Correa, P.C., Botelho, F.M., De Oliveira, A., 2015. Mechanical properties of tomatoes
663 subjected to an induced compression during storage. J. Texture Stud. 46, 293-301.

https://doi.org/10.1111/jtxs.12129.

El-Rhman, I.E.A., 2010. Physiological studies on cracking phenomena of pomegranates. J. Appl. Sci. Res. 6, 696-703.

Fenyvesi, L., Fenyvesi, D., Csatar, A., 2013. Stress analysis in fruits. Adv. Mech. Eng. 874673, 6. https://doi.org/10.1155/2013/874673.

Fahima, A., Levinkron, S., Maytal, Y., Hugger, A., Lax, I., Huang, X., Eyal, Y., Lichter, A., Goren, M., Stern, R.A., Harpaz-Saad, S., 2019. Cytokinin treatment modifies litchi fruit pericarp anatomy leading to reduced susceptibility to post-harvest pericarp browning. Plant Sci. 283, 41-50. https://doi.org/10.1016/j.plantsci.2019.02.006.

Gilbert, C., Chadoeuf, J., Vercambre, G., Genard, M., Lescourret, F., 2007. Cuticular cracking on nectarine fruit surface: Spatial distribution and development in relation to irrigation and thinning. J. Am. Soc. Hortic. Sci. 132, 583-591. https://doi.org/10.21273/JASHS.132.5.583

Gladyszewska, B., Baranowski, P., Mazurek, W., Ciupak, A., Wozniak, J., 2011. Radiation temperature of tomatoes and mechanical properties of their skin. Int. Agrophys. 25, 131-139.

Hahn, F., 2011. Fuzzy controller decreases tomato cracking in greenhouses. Comput. Electron. Agric. 77, 21-27. https://doi.org/10.1016/j.compag.2011.03.003.

Hossain, M.M., Nonami, H., 2012. Effect of salt stress on physiological response of tomato fruit grown in hydroponic culture system. Hortic. Sci. 39, 26-32. https://doi.org/10.17221/63/2011-HORTSCI.

Hernandez, V., Hellin, P., Fenoll, J., Flores, P., 2015. Increased temperature produces changes in the bioactive composition of tomato, depending on its developmental stage. J. Agric. Food Chem. 63, 2378-2382. https://doi.org/10.1021/jf505507h.

Huang, Z., Marra, F., Wang, S., 2016. A novel strategy for improving radio frequency heating uniformity of dry food products using computational modeling. Innov. Food Sci. Emerg. Technol. 34, 100-111. https://doi.org/10.1016/j.ifset.2016.01.005.

He, Z., W., 2020. Asymmetric climate warming does not benefit plant invaders more than natives. Sci. Total Environ. 742, 140624. https://doi.org/10.1016/j.scitotenv.2020.140624.

Han, X., Liu, Y., Tchuenbou-Magaia, F., Li, Z., Khojastehpour, M., Li, B., 2022. Analysis of the collision-damage susceptibility of sweet cherry related to environment temperature: A numerical simulating method. J. Food Eng. 333, 111140. https://doi.org/10.1016/j.jfoodeng.2022.111140.

Kabas, O., Celik, H.K., Ozmerzi, A., Akinci, I., 2008. Drop test simulation of a sample tomato with finite

694 element method. J. Sci. Food Agric. 88, 1537-1541. https://doi.org/10.1002/jsfa.3246.
695 Kumar, R., Kumar, A., Murthy, U.N., 2008. Heat transfer during forced air precooling of perishable food
696 products. Biosyst. Eng. 99, 228-233. https://doi.org/10.1016/j.biosystemseng.2007.10.012.
697 Karthikeyan, B., Ramanathan, S., Ramakrishnan, V., 2010. A calorimetric study of 7075 *Al/SiCp* composites.
698 Mater. Des. 31, S92-S95. https://doi.org/10.1016/j.matdes.2009.10.066.
699 Khadivi-Khub, A., 2015. Physiological and genetic factors influencing fruit cracking. Acta Physiol. Plant. 37,
700 1718. https://doi.org/10.1007/s11738-014-1718-2.
701 Koumanov, K.S., 2015. On the mechanisms of the sweet cherry *(Prunus avium L.)* fruit cracking: swelling or
702 shrinking? Sci. Hortic. 184, 169-170. https://doi.org/10.1016/j.scienta.2015.01.002
703 Khanal, B.P., Knoche, M., 2017. Mechanical properties of cuticles and their primary determinants. J. Exp. Bot.
704 68, 5351-5367. https://doi.org/10.1093/jxb/erx265.
705 Kawai, Y., Baba, T., Yoshida, M., Agravante, J.U., Del Carmen, D.R., 2018. Effects of benzyladenine and light
706 on post-harvest calamondin *(x Citrofortunella microcarpa)* fruit color and quality. Horticult. J. 87, 324-
707 328. https://doi.org/10.2503/hortj.OKD-145.
708 Lu, J., Dev, S.R.S., Raghavan, G.S.V., Vigneault, C., 2009. Simulation of a forced-air-twin-chamber for
709 measuring heat treatment uniformity in harvested tomatoes. J. Food Eng. 95, 636-647.
710 https://doi.org/10.1016/j.jfoodeng.2009.06.031.
711 Li, J., Chen, J., 2017. Citrus fruit-cracking: causes and occurrence. Hortic. Plant J. 3, 255-260.
712 https://doi.org/10.1016/j.hpj.2017.08.002.
713 Li, N., Fu, L., Song, Y., Li, J., Xue, X., Li, S., Li, L., 2019. Water entry in jujube fruit and its relationship with
714 cracking. Acta Physiol. Plant. 41. https://doi.org/10.1007/s11738-019-2954-2.
715 Li, H., Liu, G., Tian, H., Fu, D., 2021. Fruit cracking: a review. Chin. J. Biotechnol. 37, 2737-2752.
716 https://doi.org/10.13345/j.cjb.200553.
717 Li, D., Li, Z., Tchuenbou-Magaia, F., 2021. An extended finite element model for fracture mechanical response
718 of tomato fruit. Postharvest Biol. Technol. 174. https://doi.org/10.1016/j.postharvbio.2021.111468.
719 Liu, H., Han, X., Fadiji, T., Li, Z., Ni, J., 2022. Prediction of the cracking susceptibility of tomato pericarp:
720 Three-point bending simulation using an extended finite element method. Postharvest Biol. Technol. 187,
721 111876. https://doi.org/10.1016/j.postharvbio.2022.111876.
722 Laguerre, O., Denis, A., Bouledjeraf, N., Duret, S., Bertheau, E.D., Moureh, J., Aubert, C., Flick, D., 2022.
723 Heat transfer and aroma modeling of fresh fruit and vegetable in cold chain: Case study on tomatoes. Int.

J. Refrig. 133, 133-144. https://doi.org/10.1016/j.ijrefrig.2021.10.009.

Ma, F., Cheng, L., 2004. Exposure of the shaded side of apple fruit to full sun leads to up-regulation of both the xanthophyll cycle and the ascorbate-glutathione cycle. Plant Sci. 166, 1479-1486. https://doi.org/10.1016/j.plantsci.2004.01.024.

Matas, A.J., Cuartero, J., Heredia, A., 2004. Phase transitions in the biopolyester cutin isolated from tomato fruit cuticles. Thermochim. Acta 409, 165-168. https://doi.org/10.1016/S0040-6031(03)00357-5.

Marsic, N.K., Sircelj, H., Kastelec, D., 2010. Lipophilic antioxidants and some carpometric characteristics of fruits of ten processing tomato varieties, grown in different climatic conditions. J. Agric. Food Chem. 58, 390-397. https://doi.org/10.1021/jf902465e.

Mustafa, M., Syukur, M., Sutjahjo, S.H., Sobir, 2019. Inheritance of radial fruit cracking resistance in tomatoes (*solanum lycopersicum L.*), IOP Conf. Ser.: Earth Environ. Sci. 270, 012032. https://doi.org/10.1088/1755-1315/270/1/012032.

Morales-Quintana, L., Waite, J.M., Kalcsits, L., Torres, C.A., Ramos, P., 2020. Sun injury on apple fruit: Physiological, biochemical and molecular advances, and future challenges. Sci. Hortic. 260, 108866. https://doi.org/10.1016/j.scienta.2019.108866.

Pitts, M.J., Davis, D.C., Cavalieri, R.P., 2008. Three-point bending: an alternative method to measure tensile properties in fruit and vegetables. Postharvest Biol. Technol. 48, 63-69. https://doi.org/10.1016/j.postharvbio.2007.09.025.

Pek, Z., Szuvandzsiev, P., Nemenyi, A., Helyes, L., Lugasi, A., 2011. The effect of natural light on changes in antioxidant content and color parameters of vine-ripened tomato (*solanum lycopersicum L.*) fruits. Hortscience. 46, 583-585. https://doi.org/10.21273/HORTSCI.46.4.583.

Reich, P.B., Sendall, K.M., Stefanski, A., Rich, R.L., Hobbie, S.E., Montgomery, R.A., 2018. Effects of climate warming on photosynthesis in boreal tree species depend on soil moisture. Nature. 562, 263-+. https://10.1038/s41586-018-0582-4.

Sangrame, G., Bhagavathi, D., Thakare, H., Ali, S., Das, H., 2000. Performance evaluation of a thin film scraped surface evaporator for concentration of tomato pulp. J. Food Eng. 43, 205-211. https://doi.org/10.1016/S0260-8774(99)00150-8.

Sirisomboon, P., Tanaka, M., Kojima, T., 2012. Evaluation of tomato textural mechanical properties. J. Food Eng. 111, 618-624. https://doi.org/10.1016/J.JFOODENG.2012.03.007.

753 Schumann, C., Knoche, M., 2020. Swelling of cell walls in mature sweet cherry fruit: factors and mechanisms.
754 Planta 251, 65. https://doi.org/10.1007/s00425-020-03352-y.
755 Singhet, A., Shukla, A.K., Meghwal, P.R., 2020. Fruit cracking in pomegranate: extent, cause, and management
756 - a review. Int. J. Fruit Sci. 20, S1234-S1253. https://doi.org/10.1080/15538362.2020.1784074.
757 Uba, F., Esandoh, E.O., Zogho, D., Anokye, E.G., 2020. Physical and mechanical properties of locally
758 cultivated tomatoes in sunyani, Ghana. Sci. Afr. 10, e00616. https://doi.org/10.1016/j.sciaf.2020.e00616
759 Vidyarthi, S.K., El Mashad, H.M., Khir, R., Upadhyaya, S.K., Singh, S.K., Zhang, R., Tiwari, R., Pan, Z., 2019.
760 A mathematical model of heat transfer during tomato peeling using selected electric infrared emitters.
761 Biosyst. Eng. 186, 106-117. https://doi.org/10.1016/j.biosystemseng.2019.07.001
762 Woolf, A.B., Ferguson, I.B., 2000. Postharvest responses to high fruit temperatures in the field. Postharvest
763 Biol. Technol. 21, 7-20. https://doi.org/10.1016/S0925-5214(00)00161-7
764 Wang, S., Xia, J., Liu, W., Niu, S., 2009. Photosynthetic overcompensation under nocturnal warming enhances
765 grassland carbon sequestration. Ecology. 90, 2700-2710. https:// 10.1890/08-2026.1.
766 Wu, H., Ismail, M., Ding, Q., 2017. Global warming increases the interspecific competitiveness of the invasive
767 plant alligator weed, Alternanthera philoxeroides. Sci. Total Environ. 575, 1415-1422.
768 https://doi.org/10.1016/j.scitotenv.2016.09.226.
769 Wala, M., Skwarek-Fadecka, M., Kolodziejek, J., Mazur, J., Lason-Rydel, M., Krepska, M., 2022. Effect of
770 the *Fe-HBED* chelate on the nutritional quality of tomato fruits. Sci. Hortic. 293, 110670.
771 https://doi.org/10.1016/j.scienta.2021.110670.
772 Yang, Z., Zhang, L., Zhao, S., Luo, N., Deng, Q., 2020. Comparison study of static and alternating magnetic
773 field treatments on the quality preservation effect of cherry tomato at low temperature. J. Food Process
774 Eng. 43, e13453. https://doi.org/10.1111/jfpe.13453.
775 Zoratti, L., Karppinen, K., Escobar, A.L., Haggman, H., Jaakola, L., 2014. Light-controlled flavonoid
776 biosynthesis in fruits. Front. Plant Sci. 5, 534. https://doi.org/10.3389/fpls.2014.00534.